ELSEVIER

Contents lists available at ScienceDirect

Colloids and Surfaces A

journal homepage: www.elsevier.com/locate/colsurfa



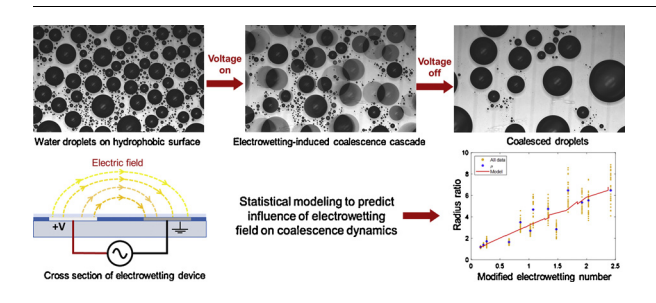
Statistical modeling of electrowetting-induced droplet coalescence for condensation applications



Enakshi Wikramanayake, Vaibhav Bahadur*

Walker Department of Mechanical Engineering, The University of Texas at Austin, Austin, TX 78712, United States

GRAPHICAL ABSTRACT



ARTICLE INFO

Keywords:
Droplets
Coalescence
Electrowetting
Regression analysis
Machine learning
Condensation

ABSTRACT

Coalescence of water droplets strongly influences dropwise condensation on hydrophobic surfaces. This work reports a study on experimental data-based statistical modeling to predict the coalescence dynamics of an ensemble of water droplets under the influence of an electrowetting (EW) field. Previous related studies have primarily used high speed visualization to characterize coalescence. However, this study uses statistical modeling to analyze the parameter space associated with EW-induced coalescence, noting that physics-based modeling of EW-induced coalescence is challenging. The objective of this study is to quantify the influence of the applied voltage, frequency of the AC waveform and the geometry of the EW device on two parameters related to droplet coalescence (droplet radius enhancement and reduction in wetted area). Multiple supervised learning techniques are used to identify dominant variables and statistically model the influence of these variables on coalescence. Data for the statistical models is obtained via image analysis from coalescence experiments.

The statistical models lead to a reference tool to predict droplet coalescence-related parameters versus the applied voltage and electrode geometry. Importantly, data analysis shows that droplet coalescence is independent of the AC frequency; this conclusion would be challenging to infer from conventional analysis. It is also seen that an EW field significantly narrows the droplet size distribution. Overall, this study leads to a detailed understanding of the factors that impact EW-induced coalescence and provides a tool (which matches experimental data) to predict the change in droplet size distribution. These findings are key to quantifying the influence of EW on condensation rates and heat transfer. This work leverages the large amount of data from experiments to develop statistical analysis-based predictive models. This approach can be utilized for predictive modeling of other data-rich but complex physical phenomena.

E-mail address: vb@austin.utexas.edu (V. Bahadur).

^{*} Corresponding author.

1. Introduction

Condensation of water vapor strongly influences the performance of equipment utilized in power generation, desalination, atmospheric water harvesting etc. The default mode of condensation on metal surfaces (typically hydrophilic) is filmwise condensation, wherein vapor condenses as a water film on the surface. The significant thermal resistance associated with this film degrades heat transfer substantially. Condensing water vapor as droplets (which roll-off on hydrophobic surfaces) can enhance heat transfer by 5-7X [1], since the thermal resistance associated with the water film is eliminated. The dynamics associated with dropwise condensation (DWC) is briefly reviewed, as it is the focus of this work. DWC begins with nucleation, followed by droplet growth via vapor condensation at the liquid-vapor interface [2-4]. When droplets grow large enough to contact neighboring droplets, the coalescence stage begins. Coalescence significantly broadens the droplet size distribution and dominates droplet growth dynamics [3]. As droplets merge and move around the surface, new droplets nucleate and grow in the dry area exposed via coalescence [3]. Throughout this process, the mean of the droplet size distribution increases, and the distribution of droplet sizes widens. When droplets grow (without coalescing), surface coverage increases; however droplet coalescence and merging will reduce surface coverage [2]. Eventually, droplets grow large enough to roll-off the surface. During roll-off, the departing droplet will capture additional fluid along its departure path, and thereby expose fresh areas for nucleation, continuing the cycle. The size at which droplets roll off is related to the capillary length, $l_c = \sqrt{\frac{y}{\rho g}}$ (γ is surface tension, ρ is density and g is gravity) which measures the relative importance of surface tension and gravitational forces. Once gravity-driven shedding begins, the system reaches a pseudo steadystate where the droplet size distribution and average droplet size remain constant [5]. Overall, the entire process of DWC is significantly influence by droplet coalescence dynamics. Many studies exist on enhancing droplet coalescence by modifying the chemistry/texture of the condensing surface [6-9].

There exist a handful of very recent studies on electrowetting (EW)-enhanced dropwise condensation. EW is a powerful tool to control droplet-based microfluidic operations such as droplet motion, generation and merging [10–14]. EW relies on the electrical modulation of the solid-liquid interfacial tension to control wettability of water and liquids like organic solvents. Application of a potential difference between a droplet on a dielectric layer and an underlying electrode increases the wettability of droplet. The voltage-dependent contact angle is modeled using the *Young-Lippmann* equation as [10]:

$$\cos\theta = \cos\theta_{eq} - \frac{C}{2\gamma_{lv}}V^2 \tag{1}$$

where θ_{eq} is the equilibrium contact angle (no voltage), γ_{lv} is the liquid-vapor interfacial tension, V is the applied voltage and C is the capacitance of the dielectric layer (under the droplet). In addition to wettability modulation, EW can be used to physically move droplets by the application of a traveling electric field over an array of electrodes (buried beneath the dielectric layer). In a recent study by the present authors [15], EW fields were used to accelerate dropwise condensation on an array of interdigitated electrodes. Droplets were observed to move to the minimum energy locations on the surface, resulting in a coalescence cascade of droplets [15,16].

In general, coalescence of droplets is a complex microfluidic phenomenon governed by various interactions occurring at the three-phase contact line and various interfaces. When droplets coalesce, initially a liquid bridge forms between the droplets, followed by the final droplet forming at the center of mass of the original droplets [2]. Studies show that during this process, contact line pinning and viscous dissipation influence the receding contact angle dynamics more strongly than advancing contact line dynamics [17]. Also, the two merging droplets

leave behind fresh dry area for nucleation to occur. *Modeling the physics associated with all these interactions is very challenging.* The challenges are significantly amplified when condensation is influence by EW, as the nature of the electric field will also come in play. It is noted that the electric field distribution will itself be altered (in a transient sense) by droplet coalescence. Additionally, the penetration of the electric field lines inside electrically conducting water droplets also depends significantly on the frequency of the applied AC EW waveform [14]. Analytical or computational predictions of EW-accelerated coalescence are challenging and of limited use due to limitations in current understanding of the underlying physics and lack of knowledge of parameters to accurately model phenomena occurring at the three-phase line.

In view of the above challenges, the present work uses experiments coupled with statistical modeling to study EW-accelerated droplet coalescence. In particular, a parametric study is conducted to understand and model the influence of three important parameters on EW-accelerated droplet coalescence: applied voltage, frequency of the AC EW field and electrode geometry. We experimentally quantify the change in droplet size distribution upon the application of an electric field, and analyze the results using multiple statistical techniques to quantify the influence of these parameters on droplet coalescence. This approach thus leverages the large amount of data (via tracking of multiple droplets) available in condensation experiments, and uses machine learning-based approaches to develop statistical predictive models, which are grounded in EW physics.

The novelty and intellectual merit of this work is briefly summarized ahead. As background, there are very few studies on droplet dynamics during EW-influenced condensation [15,16,18,19]. These studies analyze droplet coalescence via high-speed visualization of condensed droplets. However, we take a different approach, and use statistical modeling to analyze EW-induced droplet coalescence. We note that our approach takes advantage of the large quantities of data available via experiments. We also note that machine learning tools such as support vector machines, neural networks etc. have been used in studies on various microfluidic applications [20-22]. Statistical analysis has also been used to model droplet coalescence in atmospheric sciences [23,24]. However, there is no prior study on the use of any machine learning technique to study electrically enhanced coalescence of droplets. This study uses machine learning-based statistical modeling, which offers the following advantages. Firstly, machine learning tools are used for parameter shrinkage to reduce the complexity of the system; direct analysis of data would not enable the same findings as those obtained in our study. Secondly, we use the predictions from the statistical models to propose a reference tool to predict changes in droplet size distribution due to coalescence. It is noted that our modeling is grounded in EW physics, and shows a good match with experimental data. We note that while the analysis is conducted for a specific EW configuration, the conclusions and the current approach (experimental data-based statistical modeling) can be adopted to a wide variety of configurations.

2. Experimental procedures

Indium Tin Oxide (ITO) coated glass slides were used as the substrates for fabricating EW devices. Standard photolithography and plasma etching processes were used to pattern an interdigitated electrode layout (Fig. 1a). Details of the fabrication processes are included in the supplementary information. A co-planar electrode geometry with interdigitated electrodes stripes was used, with the two sets of electrodes located adjacent to each other (Fig. 1a). The two sets of electrodes were connected to the high voltage and ground ends of a signal generator and amplifier to generate an electric field in the gap between adjacent electrodes. Fig. 1b shows the cross section of the condensation surface. A 5 μ m layer of SU-8 2005 was spin-coated on the entire surface as the EW dielectric. This dielectric layer is critical to the performance

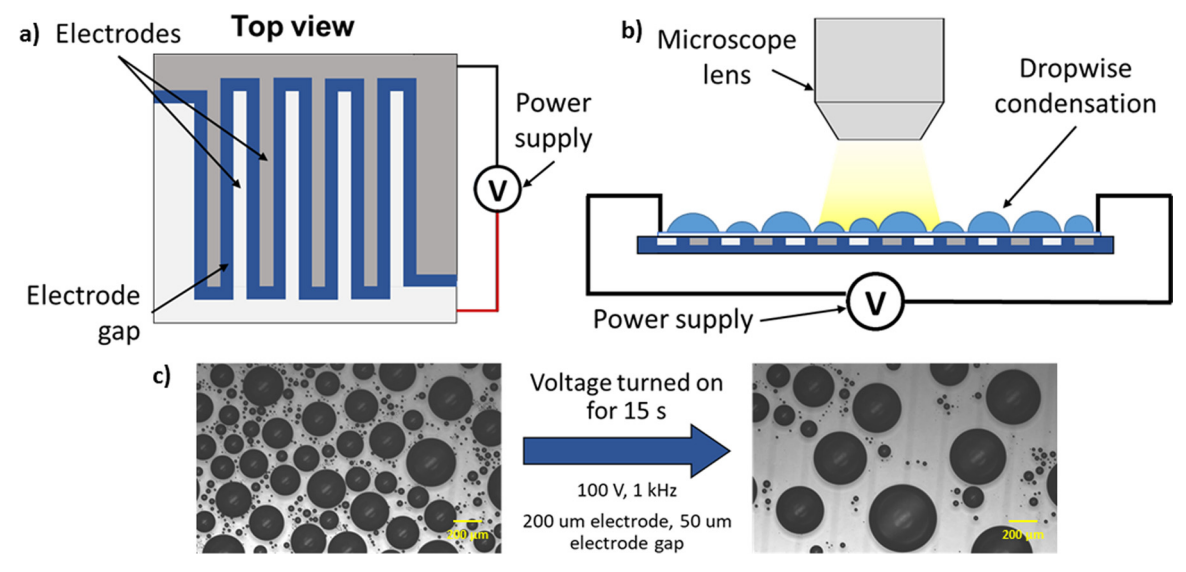


Fig. 1. Schematic showing the arrangement of interdigitated electrodes (high voltage electrodes in white and ground electrodes in dark grey). (b) Cross section of device with droplets on top. (c) Droplet coalescence due to the influence of an EW field applied for 15 s.

of EW systems, as it stores the electrostatic energy for droplet actuation. Finally, a 100 nm layer of Teflon was spin-coated to act as the hydrophobic layer.

Next, the experimental procedure is briefly described. It is noted that the primary objective of this study is to investigate the influence of key EW parameters on coalescence of droplets (and not roll-off). The starting ensemble of droplets (to be coalesced) was obtained by spraying water using a commercial room humidifier on horizontally oriented surfaces. Droplet size distributions obtained via this procedure were remarkably consistent in multiple repetitions, and the mean droplet size of the initial distribution was $79\,\mu\mathrm{m}\,\pm\,9\,\mu\mathrm{m}.$ It is striking to observe that the obtained droplet size distribution is similar to that obtained in classical dropwise condensation experiments [25]. This finding thus justifies the utility of the present approach for modeling coalescence in dropwise condensation. This approach also enables the collection of large data sets for statistical analysis, noting that dropwise condensation experiments would involve much longer durations.

Post droplet-deposition, the surface was continuously visualized using the $5\times$ magnification lens of a Nikon Eclipse LV150N optical microscope. The EW field was then turned on for 15 s, during which droplet coalescence dynamics were recorded at 100 fps. It is shown subsequently, that 15 s is long enough for all coalescence events to be completed. The droplet size distribution before and after the application of an EW field was compared to quantify the extent of coalescence. Post-processing involved using a MATLAB code to count the number and size of droplets on the surface (circle finder image processing script). The current software and imaging capabilities allowed the detection of droplets as small as $5\,\mu m$. Droplets were assumed to have a spherical cap geometry, with a contact angle of 120° in the absence of an EW field. Droplet radii before and after the application of voltage were calculated and used in the statistical analysis.

Next, the three experimental parameters varied in this study are briefly described. Firstly, three different electrode geometries were characterized with electrode widths of $50\,\mu m$, $100\,\mu m$ and $200\,\mu m$; spacing between adjacent electrodes was maintained at $50\,\mu m$ in all devices. The electrode:electrode gap ratios were thus 1, 2 and 4. These geometrical parameters influence the inter-electrode field and the penetration height of the electric field outside the surface. The second parameter varied was the applied voltage. Experiments were conducted at three different voltages ($100\,V$, $200\,V$, $300\,V$). These voltages were higher than the threshold voltage for EW actuation, but lesser than the saturation voltage, as observed from the EW curve. The third parameter

varied was the frequency of the applied AC waveform. Experiments were conducted at 1 Hz, $10\,\mathrm{Hz}$, $50\,\mathrm{Hz}$, and $1\,\mathrm{kHz}$ as they capture various types of droplet motion (ranging from translation of droplets to shape variation). It is noted that all experiments were repeated $10\,\mathrm{times}$. Overall, this procedure highlights the experimental rigor involved in this study, and the efforts to get sufficient data for meaningful statistical analysis.

3. Description of statistical analysis-based modeling approach

The goal of this study is to identify the relative influence of three input parameters on droplet coalescence; this was achieved by estimating two coalescence-related parameters before and after the application of an EW field. The first parameter is the ratio of the area-averaged radius $<\widehat{R}>=\frac{\sum_r r^3}{\sum_r r^2}$, after and before the application of the EW field. The second parameter is the ratio of the reduction in the wetted area to the initial wetted area. The wetted area is the fraction of the surface covered by liquid, and will reduce with increasing coalescence. Both these parameters (also referred to as output variables in the model) were estimated via image analysis after every experiment.

Three statistical techniques (Ridge regression, Lasso regression and Random Forest) were used to analyze the resulting data sets, and to identify the relative influence of the three input parameters on droplet coalescence. We note that the use of three techniques is not an essential practice; however multiple techniques were used to develop additional confidence in our findings (by comparing the results obtained from these techniques). All these three techniques are supervised learning methods, and are widely used in statistical modeling for feature selection or shrinkage [26]. Ridge regression is an extension of linear regression analysis and imposes a penalty to the expression that minimizes the sum of least squares (which is the cost function associated with linear regression), causing variable shrinkage. The penalty is imposed to the total size of the coefficients such that more important predictors will have higher coefficients and less important predictors will have lower coefficients, based on the magnitude of the applied penalty [27,28]. Ridge regression minimizes the cost function as:

$$\sum_{i=1}^{N} \left(y_i - \sum_{j} x_{ij} \beta_j \right)^2 + \lambda \sum_{j=1}^{P} \beta_j^2$$
 (2)

where the first term is the cost function associated with least squares, and the second term is the additional penalty term. Here, x includes the set of independent variables and y is the dependent variable to be

predicted. λ is the applied penalty which can be optimized; the model solves for the parameter β in order to minimize the cost function ·

Another method of variable selection is Lasso regression. Similar to Ridge regression, Lasso regression imposes a penalty term to the sum of squares minimization, where the penalty term takes the form of $\lambda \sum_{j=1}^p |\beta_j|$. This penalty term shrinks the unimportant variable coefficients to zero, eliminating them from the model [27,29,30] which is a significant benefit of Lasso regression over Ridge regression. This makes Lasso regression an advantageous screening tool to identify the most correlated variable, creating a more sparse problem with fewer coefficients [29]. Additionally, in Lasso regression, the variable selection process is continuous and more stable, making it more computationally feasible for higher dimensional data.

The Random Forest method is widely used in statistical data science regression studies. Random Forests consist of several decision trees which are models that learn to split the dataset into smaller and smaller subsets to predict the target values. During this process, many hyper parameters (such as the number of decision tress in the forest and the number of features considered by each tree when splitting a node) must be optimized in order to reduce the error between the training and predicted data [26]. Presently, besides optimizing the Random Forest model to minimize the error, we also consider the importance of the input features. Feature importance is calculated as the decrease in node impurity weighted by the probability of reaching that node. The node probability is estimated as the ratio of the number of samples that reach the node to the total number of samples. This method identifies the input variables which contribute the most to building the decision trees in the forest; these will also impact the output variables accordingly.

After identifying the significant input parameters (geometry and voltage, as described ahead), the next step in the present work was to select a tool to accurately model and predict the relationship between the significant input parameters and output parameters. Since this study was about regression analysis, we used the Support Vector Regression (SVR) and Kernel Ridge Regression (KRR) methods.

SVR is based on Support Vector Machines (SVM) which is a classification method that uses hyperplanes to best separate the features into different domains. Alternatively, SVR is a regression method where, like SVM, bounds are defined within which the error can lie. The goal of SVR is to find these bounds in the form of a function that at most deviates by ϵ from the target values for all the training data. Here ϵ is user specified threshold parameter that determines the threshold within which the error can exist; the error cannot deviate larger than the set value. The goal of this method is to ensure the errors do not exceed the threshold ϵ value. In SVR, the inputs are first nonlinearly mapped into a high dimensional feature space wherein they are correlated linearly with the output [31]. Such a linear regression in high-dimensional feature space reduces the algorithm complexity, enabling high predictive capabilities of both training and unseen test examples.

KRR is an extension of least square regression which solves over-fitting and multicollinearity problems associated with least square methods by integrating Ridge regression and kernel methods [32]. The form of the model is very similar to SVR; however, the loss function uses a squared error. Both SVR and KRR use a kernel function which maps the non-linear data to a higher dimensional linear space to reduce the complexity of solving the problem. Several different kernel functions exist, including linear and polynomial. One of the more frequently used kernel functions is the radial basis function (rbf) described as [33]:

$$(x_i, x_j) = \exp\left(-\frac{(x_i - x_j)^T (x_i - x_j)}{2\sigma^2}\right)$$
 (3)

where x_i and x_j represent the two input vectors and σ is a free parameter which can be expressed as $\gamma = \frac{1}{2\sigma^2}$ such that γ sets the spread of the kernel

The methodology adopted in this study involved collecting the training and testing data and then preparing the data by removing any

obvious outliers. The data was then scaled linearly before using it in modeling algorithms. For variable selection a model parametric sweep was conducted to identify the best model hyperparameters to minimize the error between the training and testing data [31]. Once the optimized hyperparameters were selected, k-fold cross validation (where k=10) was conducted such that the average absolute error was minimized and the correlation coefficient was enhanced [30,32]. The training and testing data were compared so as to minimize the rootmean-square error (RMSE) and maximize the coefficient of determination (R^2). It is noted that all the statistical analysis conducted in this work was done in Python.

4. Results

The first step in our analysis involved eliminating the possibility of multi-collinearity between input descriptors. A Pearson's coefficient correlation was used to compare the correlation coefficients between the input and output variables. The three input variables (voltage (V), frequency (f) and electrode width (e)) can be captured by three nondimensional numbers: (i) electrowetting number $\zeta = \frac{\varepsilon V^2}{2\nu d}$, (ii) dimensionless relaxation time $\tau = \frac{\sigma_{|\varepsilon}}{\omega}$ ($\omega = 2\pi f$), and (iii) geometry ratio $L = \frac{\text{width}_{electrode}}{\text{width}_{electrode} \text{ gap}} = \frac{e}{g}. \text{ Here } \varepsilon = \varepsilon_d \varepsilon_0, \text{ where } \varepsilon_d \text{ is the electrical permit$ tivity of the dielectric, ε_0 is the electrical permittivity of vacuum, γ is the liquid-vapor surface tension, d is the dielectric layer thickness, σ is the electrical conductivity, e is the electrode width and g is the spacing between the electrodes. The two output variables are the area-weighted radius enhancement ratio $R = \frac{\widehat{R}_f}{\widehat{R}_l}$ and the normalized reduction in wetted area $A = \frac{A_{wetted,i} - A_{wetted,j}}{A_{wetted,i}}$. Fig. 2 shows that all the input descriptors have very low statistical correlation coefficients between each other, indicating that they are independent of each other and that there is no multicollinearity between these variables. Additionally, higher correlation coefficients are seen between two input variables (ζ and L) and the output variables.

The next step in the analysis was parameter selection, where parameter shrinkage was used to identify the input parameters which dominantly influence the output parameters during droplet coalescence. This was implemented by employing the variable selection methods; Ridge regression, Lasso regression and Random Forest importance selection. Such techniques are used to reduce the complexity of the problem being studied. During this analysis the three non-dimensional variables were analyzed against the output variables and the corresponding coefficients were compared. Fig. 3 shows that coefficients from both regression methods and the Random Forest importance

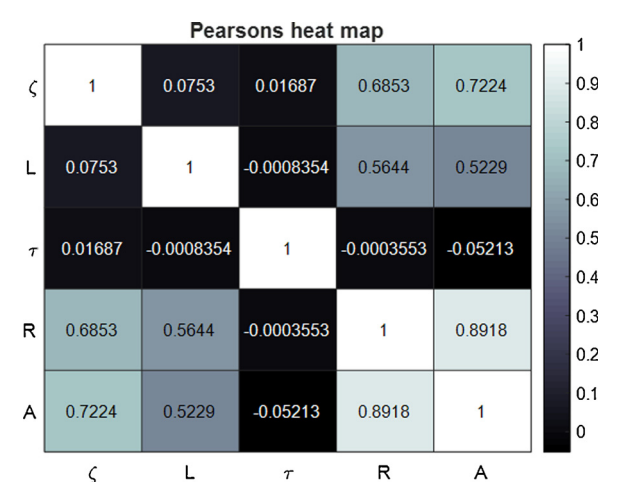
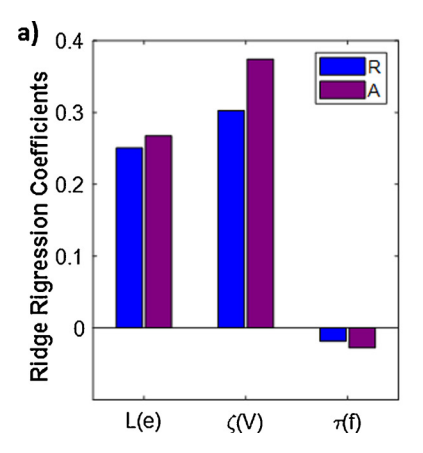
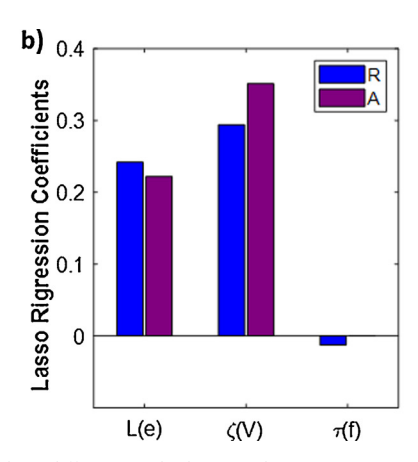


Fig. 2. Heat map showing Pearson's correlation coefficients between the three input variables (ζ (V), L (e), τ (f)) and the two output variables, R and A.





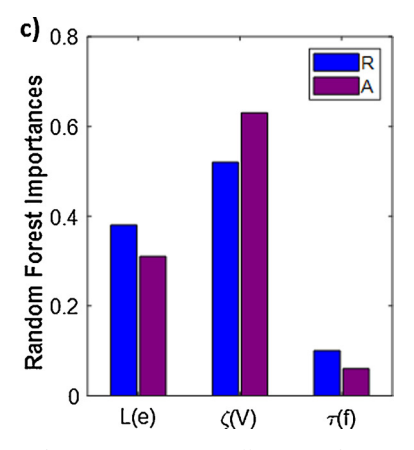


Fig. 3. Parameter selection and shrinkage conducted via three different methods: (a) Ridge regression coefficients, (b) Lasso regression coefficients and (c) Random Forest importance. Blue and purple bars indicate coefficients associated with the radius ratio and change in the wetted area, respectively.

assign high significance to $\zeta(V)$ and L(e), indicating that both these parameters strongly contribute to the change in radius and wetted area. The radius ratio is found to be most dependent on ζ (V) and L(e), which have ~50% and ~40% Random Forest importance, respectively. Similarly, the reduction in wetted area also shows strong dependence on ζ (V) and L(e). In this case, ζ (V) has a Random Forest importance of ~65% indicating the change in wetted area most strongly depends on the applied voltage, followed by the electrode geometry, L(e), which has an importance of $\sim 35\%$. Importantly, Fig. 3 shows that the radius ratio and reduction in wetted area are independent of $\tau(f)$, as the corresponding correlation coefficients are negligible. The correlation coefficients for ζ (V) and L (e) are ~10X greater than that of τ (f) for change in radius. Lasso regression completely eliminates $\tau(f)$ as a dependent variable for the change in wetted area. Similar results are seen in the Random Forest classification where frequency dependence is given < 10% of the overall importance for both output parameters. It is important to note that analyzing raw data alone was insufficient to deduce these conclusions that were clearly shown in Fig. 3.

A key conclusion from Fig. 3 is that the AC frequency does not influence coalescence dynamics significantly (at least not in the currently used frequency range of 1 Hz to 1 kHz, which is widely used in AC EW experiments). Such conclusions are challenging to arrive at from physics-based models, which would need to account for complex phenomena such as contact angle hysteresis and the electromechanical response of a liquid to a time varying electric field. This finding is also challenging to predict from high speed visualization of droplets. Indeed, our recent study [15] showed that the AC frequency strongly influences the nature of droplet motion (translation versus shape oscillation), as well as the orientation of droplets on the electrodes.

The physics underlying the predicted frequency-invariance of coalescence dynamics can be better inferred by analyzing the temporal occurrence of coalescence events. Droplet coalescence is not a continuous process as clearly identified in our previous study on dropwise condensation [15]. Instead coalescence is observed to occur in bursts (reported later in this study), with a large number of coalescence events occurring in a very short time interval. Post coalescence, droplets will grow via additional condensation (as observed in previous studies [3,15,16]), leading to another 'coalescence cascade' at a later time instant. Such periodic coalescence cascades will not occur in the current study, and only a single coalescence cascade is observed (Fig. 6). Coalescence parameters R and A depend on this cascade phenomena, which in turn depends on the applied voltage and device geometry, but not significantly on the AC frequency. In summary, the current findings indicate that while the AC frequency will influence the translation and oscillatory motion of individual droplets [15,19], it does not influence the change in the droplet size distribution, before and after the field is applied.

It is noted that this finding of droplet coalescence being AC frequency-independent, underscores the importance of statistical analysis for such complex multi-physics problems. The applied voltage and electrode geometry are two parameters which strongly influence droplet coalescence dynamics. It is noted that this conclusion might not be applicable to droplet shed-off (which is not the focus of the current study), but only for coalescence.

Based on the findings of the variable shrinkage analysis, we next develop a model to predict the radius enhancement ratio R and normalized reduction in wetted area A, as a function of the applied voltage (V) and geometry (electrode width e). Both these parameters can be combined into a parameter similar to the EW number [10], but with the capacitance term modified to incorporate for electrode geometry. The modified, non-dimensional EW number which includes the voltage and the electrode geometry takes the form:

$$\eta(V,e) = \frac{c/w}{\gamma_{lv}} V^2 \tag{4}$$

where C_{w} is the capacitance per unit width. For the present co-planar electrode geometry, the capacitance can be estimated as [34]:

$$C_{W}' = \frac{2\varepsilon_{0}\varepsilon_{d}l}{\pi A} \ln \left[\left(1 + \frac{e}{g} \right) + \sqrt{\left(1 + \frac{e}{g} \right)^{2} - 1} \right]$$
 (5)

Next, a statistical and data science-based model to predict the relationship between R and A versus $\eta(V,e)$, is developed. Since this is a regression-based analysis, the regression models SVR and KKR are used to compare the predicted values with experimental data. As an additional validation, we also consider the mean and standard deviation of each set of experiments, independent of the frequency, by fitting a probability density function (PDF) to the respective data sets. This step is important as the data has scatter, especially at larger values of $\eta(V,e)$. The error associated with the statistical models is detailed in Tables 1 and 2 for the radius enhancement ratio (R) and normalized reduction in wetted area ratio (A), respectively. The predictive accuracy

Table 1Compilation of errors (in the form of RMS and R² values) for various models predicting the radius enhancement ratio of coalescing droplets.

Model	RMSE	R^2
Linear Regression	1.14	0.72
Polynomial Regression, degree 2	1.25	0.69
Polynomial Regression, degree 3	1.48	0.63
SVR - Linear	1.12	0.72
SVR - RBF	1.89	0.53
Kernel Ridge - Linear	1.31	0.73
Kernel Ridge - RBF	1.56	0.63

Table 2 Compilation of errors (in the form of RMS and R^2 values) for various models predicting the normalized reduction in wetted area associated with droplet coalescence.

Model	RMSE	\mathbb{R}^2
Linear Regression	0.018	0.65
Polynomial Regression, degree 2	0.014	0.73
Polynomial Regression, degree 3	0.014	0.71
SVR - RBF	0.019	0.61
SVR - Poly deg 2	0.055	0.36
SVR - Poly deg 3	0.055	0.36
Kernel Ridge - RBF	0.014	0.71
Kernel Ridge - Poly deg 2	0.015	0.74
Kernel Ridge - Poly deg 3	0.014	0.72

of each model is evaluated by comparing the RMSE and R^2 values between the predicted and experimental data, with models with low RMSE and higher R^2 values representing a more favorable match. Detailed comparisons of these predictive models with the experimental data are provided in the supplementary information.

Based on the results for radius enhancement ratio as a function of $\eta(V,e)$ (Table 1), the first important observation is that the data follows a linear trend. This is concluded because the linear regression fit shows higher accuracy when compared to the polynomial curve fits. Following this observation, the linear kernel and the rbf kernel are used in the statistical models. When comparing the predictive accuracy of the two kernel methods, the linear kernel shows a lower RMSE and higher R^2 for both methods, implying that the linear kernel can more accurately capture the trend between $\eta(V,e)$ and R. The rbf kernel models attempt to follow the highest probability density in the data at each point with respect to $\eta(V,e)$, and can compromise the accuracy with the entire data set. The lowest RMSE and highest accuracy corresponds to the SVR model with the linear kernel, which shows the best match with experimental data.

Based on the results for normalized reduction in wetted area as a function of $\eta(V, e)$ (Table 2), it is seen that 2nd and 3rd degree polynomial curves are a better fit compared to a linear model (based on the resulting RMSE and R² values). Polynomial fits with greater than 3rd order did not show any improvement in accuracy. Hence, the statistical models compare the rbf kernels with 2nd and 3rd degree polynomial kernels. When comparing the predictive accuracy of the two statistical models, Table 2 shows that KRR performs significantly better than the SVR model. Although the SVR model used with the rbf kernel has a low RMSE, the two polynomial kernels show poor agreement with the experimental data. Alternatively, the KRR model shows good accuracy with low RMSE and high R2 values for all kernel types. The best predictability is seen with the KRR model using the 2nd degree polynomial kernel. Overall, the rbf kernels perform well with both models, however, the KRR model shows the most consistent predictive accuracy for different kernel types. It is noted that machine learning algorithms with kernel functions are more accurate (in terms of reducing error between experimental data and modeling-based prediction) compared to classical linear or polynomial regression. This highlights the utility of using statistical machine learning algorithms for the analysis of coalescence, compared to classical regression methods.

Fig. 4 compares the models having high predictive accuracy with the corresponding experimental data for R (4a) and A (4b). Fig. 4a shows that the SVR model with the linear regression kernel predicts the linear trend in the data reasonably well. Extrapolating the model to $\eta(V,e)=0$ (no electric field) yields $R\sim1$ implying no change in droplet radii (as expected). Fig. 4b shows the experimental data for normalized reduction in wetted area compared to the KRR with second order polynomial kernel. A good match between model and data is seen, as captured by the low RMSE and high R^2 values. Again, extrapolating this model to $\eta(V,e)=0$ shows that $A\sim0$ which is expected.

Details of all other predictive models and comparisons with their optimized hyperparameters are included in the supplementary information

The predictions of statistical modeling, as captured in Fig. 4a, indicate that the radius ratio, R linearly increases with $\eta(V,e)$ with a gradient of 2.5. This implies that if an electric field is provided such that $\eta(V,e)=2$, the initial average radius in the distribution will increase by $5\times$. The reduction in wetted area does not follow a linear trend (Fig. 4b), and the model can estimate the electric field to maximize the reduction in wetted area. Fig. 4b shows $\eta(V,e)\sim 1.75$ yields the maximum reduction in wetted area of $\sim 70\%$. The utility of this model lies in the ability to predict the electric field, (captured via $\eta(V,e)$), required to yield a desired droplet size distribution from an initial distribution. As an illustration, a 2X increase in average droplet radius would require an electric field corresponding to $\eta(V,e)=0.75$ (based on the reference given in Fig. 4a).

An examination of Fig. 4 also shows that the data has scatter which can be attributed to a combination of experimental uncertainty and the stochastic nature of coalescence dynamics under electric fields. Additionally, the scatter increases at higher values of $\eta(V,e)$, which can be attributed to contact angle saturation, whereby the droplet stops responding to the electric field [10,12]. Even with the scatter in Fig. 4, there is a clear trend showing the influence of $\eta(V,e)$ on the radius ratio enhancement and the normalized reduction in wetted area. It is reiterated that both these variables quantify droplet coalescence and the resulting change in the droplet size distribution upon the application of an EW field.

Fig. 4 quantifies the influence of $\eta(V,e)$ on R and A, which are directly related to the droplet size distribution. We can also quantify the influence of $\eta(V,e)$ on droplet size distribution more directly by analyzing the influence of the EW field on the spread of the droplet size distribution. The spread is defined as the standard deviation of the droplet size distribution relative to the area average radius as:

$$S_i = \frac{\sigma_i}{\hat{R}_i} = \frac{standard\ deviation}{area\ average\ radius} \tag{6}$$

A large value of S_i indicates that a wide range of droplet sizes exist relative to \hat{R}_i , whereas a smaller value of S_i indicates that most of the droplets are of similar size to \hat{R}_i . The change in S_i before and after the application of the EW field is quantified as:

$$S = S_F/S_I \tag{7}$$

where S_F and S_I are the final and initial distribution spreads. Fig. 5 shows the change in S as a function of $\eta(V,e)$. For small values of $\eta(V,e)$, the change in the distribution spread is negligible ($S\sim 1$). However, after $\eta(V,e)=0.75$, the change in the spread shrinks by $\sim 50\%$, indicating that the distribution of droplets reduces significantly and many droplets are closer in size to the mean radius. The spread ratio maintains this trend for larger values of (V,e). Combining this information with the results depicted in Fig. 4 makes it clear that an increase in $\eta(V,e)$ will not only increase the droplet size and reduce the wetted area, but also narrow the droplet size distribution, and reduce the number of droplets on the surface.

5. Discussions

We now discuss the transients associated with EW-induced droplet coalescence, noting that the model depicted in Fig. 4 shows the overall change in droplet coalescence parameters. The time-dependent average radius after applying the EW voltage was estimated via the image analysis procedure described previously. Variable selection analysis shows that the transient change in *R* is independent of frequency but strongly dependent on the applied voltage, electrode width and time (details provided in the supplementary information). Arriving at this conclusion would not have been possible without the use of variable selection tools, due to the high dimensionality of the data. Fig. 6 shows

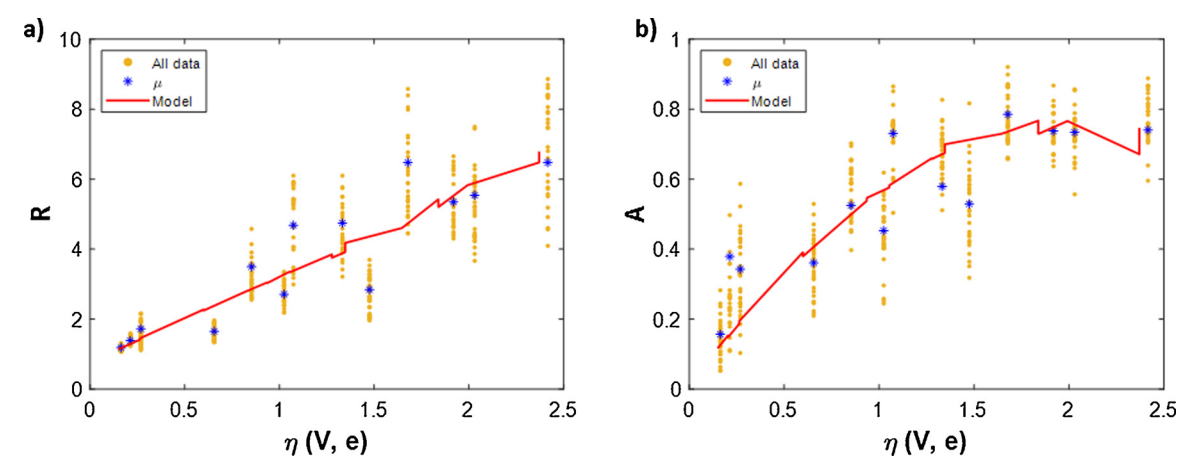


Fig. 4. Comparing experimental data (orange), mean values (dark blue) and statistical model predictions (red) for (a) radius enhancement ratio using SVR with linear kernel ($\mathcal{E} = 1e-05$, C = 1000) and (b) normalized wetted area reduction using KRR with second order polynomial kernel ($\mathcal{E} = 1e-05$, C = 1000) and (b) normalized wetted area reduction using KRR with second order polynomial kernel ($\mathcal{E} = 1e-05$, $\mathcal{E} = 1000$).

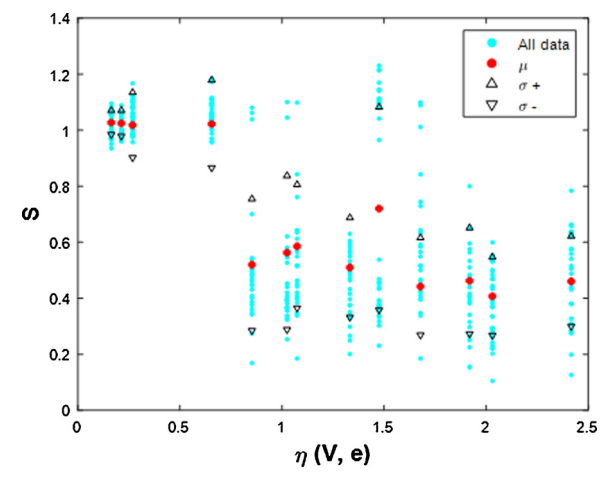


Fig. 5. Change in the spread in droplet size distribution versus $\eta(V, e)$.

the voltage-dependent, transient, radius enhancement ratio for three different electrode geometries. As expected, the radius increases faster at higher voltages due to larger electrostatic forces to promote coalescence. Additionally, a large jump in radius ratio from 100 V (threshold

voltage) to 200 V is observed. Larger electrode widths also show a greater radius. The 50 μ m electrode width geometry enables a maximum radius enhancement ratio of $R \sim 3$, whereas the 200 μ m electrode width geometry enables an enhancement of R = 5.5–6. It is also noted that most of the coalescence events occur in the first 5 s after the field, after which the average radius generally plateaus out. Such a coalescence cascade was also reported in other recent studies [15,16]. This finding also justifies our use of a 15 s interval to quantify the influence of EW fields on coalescence dynamics.

In the previous section, we highlighted the accuracy of machine learning-based models in predicting changes in droplet size distribution during an EW driven coalescence cascade. Next, we discuss the physics underlying the observed dependence of coalescence parameters on the applied voltage (V) and electrode geometry (captured by electrode width (e)); this can be considered as further validation of the results obtained by the statistical models. The observed data and the models show that higher voltages and higher electrode widths enhance droplet coalescence. This can be explained by considering the electrowetting curve (contact angle (CA) versus voltage) for sessile water droplets [10,12]. Fig. 6 shows the electrowetting curves for two different electrode widths as obtained from the Young-Lippman equation (Eq. (1)) and via experiments with sessile water droplets. As expected, droplets spread with increasing voltage till the onset of CA saturation [12].

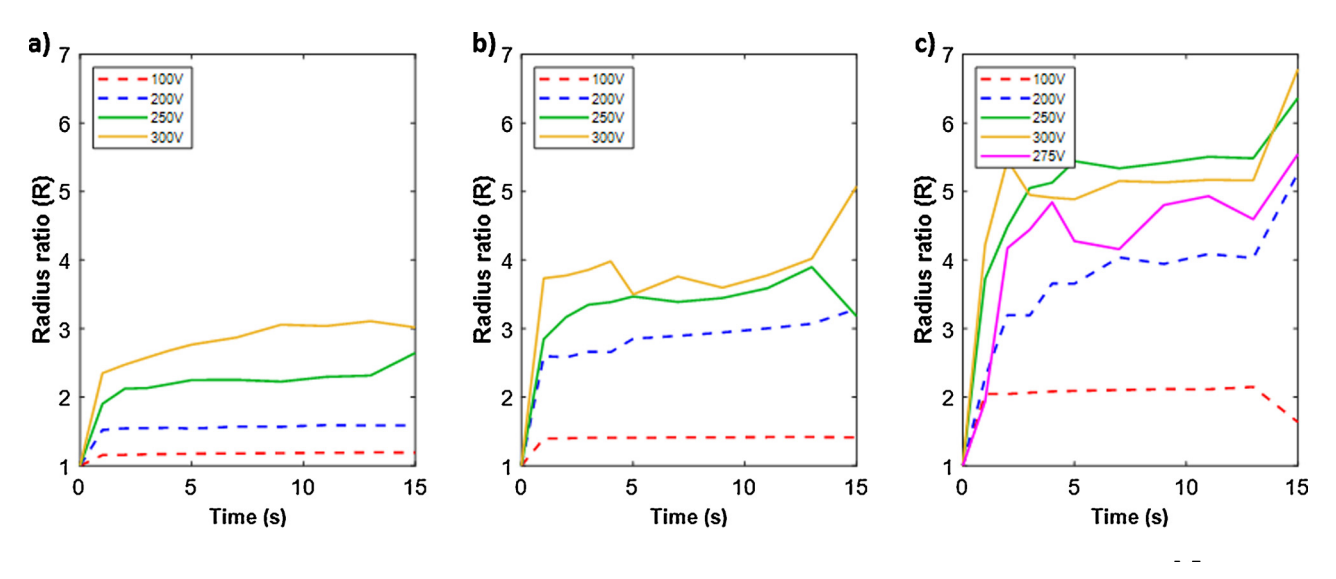


Fig. 6. Transient change in radius enhancement ratio R for a period of 15 s after the application of EW voltages on devices with electrode widths (a) 50 μm, (b) 100 μm and (c) 200 μm. Most coalescence events occur immediately after the application of an EW field leading to a coalescence cascade.

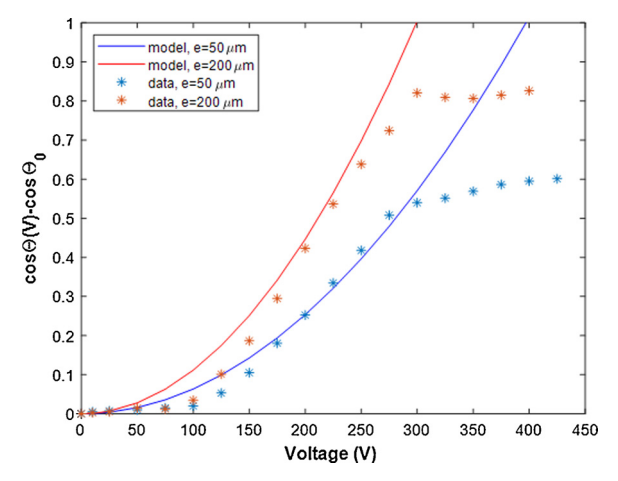


Fig. 7. Electrowetting curve showing the change in contact angle with applied voltage for two electrode widths.

Additionally, Fig. 7 shows that a larger electrode width yields a larger change in CA for a specified voltage; this is directly related to the increased capacitance associated with the larger electrode width as quantified in Eq. (5). [34]. Since droplet spreading ultimately leads to droplet coalescence, the radius enhancement ratio is expected to increase with higher voltages and electrode widths. Similarly, the reduction in wetted area also increases with an increase in the voltage and electrode width. However, the reduction plateaus, as per Fig. 4b, even though the radius enhancement ratio is increasing. This can be explained by the CA saturation phenomena, wherein the wetted area becomes independent of the applied voltage above a certain applied voltage.

Finally, the utility of this study for condensation heat transfer is briefly discussed. There are a few recent studies [16,18,35] on EW enhanced droplet condensation, which involve condensation occurring under a continuously applied electric field. A continuous electric field is not a strict requirement; periodically applied electric fields can also result in significant enhancement in condensation. This study will directly benefit any such 'electrical intervention' strategies to enhance dropwise condensation. The output parameters tracked in this study are critical to overall performance. The growth rate of droplets via coalescence is significant since the enhancement mechanism is about reorganizing the condensate into high volume droplets that can then shed-off. The droplet size is also a critical parameter in the estimation of the thermal resistance associated with heat transfer [8]. The reduction in wetted area determines the rate at which condensation will reoccur on the surface. Overall, this study represents a new approach to predicting the performance of EW-enhanced dropwise condensation. This study can benefit other applications which rely on droplet manipulation via EW like anti-fouling or self-cleaning [36].

6. Conclusions

This is the first reported study of EW-induced droplet coalescence, which uses machine learning-based statistical algorithms to develop experimental data-based predictive models. This approach contrasts with previous studies, which analyze coalescence patterns via high-speed visualization. The attractiveness of this approach lies in the challenges involved in developing accurate physics-based models for complex microfluidic systems. This approach also leverages the large (and easily obtained) amount of data available in condensation experiments (via tracking a multitude of droplets). The models developed predict the change in droplet radius and wetted fractions as a function of the applied voltage and electrode geometry. Importantly, the results can provide additional physical insights that would be challenging to infer from conventional data analysis, such as droplet coalescence being

independent of the AC frequency, and the EW-influenced narrowing of droplet size distributions. Additionally, machine learning regression models using kernel methods show better fit with experimental data than classical regression techniques. We note that while our analysis involves the use of statistical techniques, it is grounded in the basic physics associated with EW. More broadly, this study motivates the application of the current approach for predictive modeling of other complex multiphysics systems, which lend themselves to large quantities of experimental data.

Declaration of Competing Interest

The authors declare that they have no conflict of interest.

CRediT authorship contribution statement

Enakshi Wikramanayake: Methodology, Investigation, Data curation, Formal analysis, Visualization, Writing - original draft. **Vaibhav Bahadur:** Conceptualization, Methodology, Writing - review & editing, Supervision.

Acknowledgements

The authors acknowledge National Science Foundation grant no. CBET- 1805179 for supporting this work.

Appendix A. Supplementary data

Supplementary material related to this article can be found, in the online version, at doi:https://doi.org/10.1016/j.colsurfa.2020.124874.

References

- E. Schmidt, W. Schurig, W. Sellschopp, Experiments on the condensation of water vapor in film and drop form, Eng. Mech. Thermodyn. 1 (2) (1930) 53–63.
- [2] R.N. Leach, F. Stevens, S.C. Langford, J.T. Dickinson, Dropwise condensation: experiments and simulations of nucleation and growth of water drops in a cooling system. Langmuir 22 (3) (2006) 8864–8872.
- [3] J.E. Castillo, J.A. Weibel, S.V. Garimella, The effect of relative humidity on dropwise condensation dynamics, Int. J. Heat Mass Transf. 80 (2015) 759–766.
- [4] N. Watanabe, M. Aritomi, A. Machida, Time-series characteristics and geometric structures of drop-size distribution density in dropwise condensation, Int. J. Heat Mass Transf. 76 (September) (2014) 467–483.
- [5] J.B. Boreyko, C. Chen, Self-Propelled Dropwise Condensate on Superhydrophobic Surfaces, Phys. Rev. Lett. 184501 (October) (2009) 2–5.
- [6] D.M. Anderson, et al., Using amphiphilic nanostructures to enable long-range ensemble coalescence and surface rejuvenation in dropwise condensation, ACS Nano 6 (4) (2012) 3262–3268.
- [7] K. Rykaczewski, A.T. Paxson, S. Anand, X. Chen, Z. Wang, K.K. Varanasi, Multimode Multidrop Serial Coalescence Effects during Condensation on Hierarchical Superhydrophobic Surfaces, Langmuir 29 (3) (2013) 881–891.
- [8] N. Miljkovic, R. Enright, E.N. Wang, Modeling and Optimization of Superhydrophobic Condensation, J. Heat Transfer 135 (11) (2013) 111004.
- [9] R. Enright, N. Miljkovic, J. Sprittles, K. Nolan, R. Mitchell, E.N. Wang, How coalescing droplets jump, ACS Nano 8 (10) (2014) 10352–10362.
- [10] F. Mugele, J.-C. Baret, Electrowetting: from basics to applications, J. Phys. Condens. Matter 17 (July (28)) (2005) R705–R774.
- [11] G. Lippmann, Relations entre les phénomènes électriques et capillaires, Gauthier-Villars, 1975.
- [12] L. Chen, E. Bonaccurso, Electrowetting From statics to dynamics, Adv. Colloid Interface Sci. 210 (August) (2014) 2–12.
- [13] V. Bahadur, S.V. Garimella, An energy-based model for electrowetting-induced droplet actuation, J. Micromechanics Microengineering 6 (2006) 1494–1503.
- [14] N. Kumari, V. Bahadur, S.V. Garimella, Electrical actuation of electrically conducting and insulating droplets using ac and dc voltages, J. Micromechanics Microengineering 18 (10) (2008).
- [15] E.D. Wikramanayake, V. Bahadur, Electrowetting-based enhancement of droplet growth dynamics and heat transfer during humid air condensation, Int. J. Heat Mass Transf. 140 (2019) 260–268.
- [16] D. Baratian, R. Dey, H. Hoek, D. Van Den Ende, F. Mugele, Breath Figures under Electrowetting: Electrically Controlled Evolution of Drop Condensation Patterns, Phys. Rev. Lett. 120 (21) (2018) 214502.
- [17] Y. Nam, D. Seo, C. Lee, S. Shin, Droplet coalescence on water repellant surfaces, Soft Matter 11 (1) (2015) 154–160.
- [18] R. Yan, C.-L. Chen, Condensation Droplet Distribution Regulated by Electrowetting,

- J. Heat Transfer 141 (11) (2019).
- [19] S. Högnadóttir, K. Kristinsson, H.G. Thormar, K. Leosson, Increased droplet coalescence using electrowetting on dielectric (EWOD), Appl. Phys. Lett. 116 (February) (2020) 073702.
- [20] G.M. Hobold, A.K. da Silva, Machine learning classification of boiling regimes with low speed, direct and indirect visualization, Int. J. Heat Mass Transf. 125 (October) (2018) 1296–1309.
- [21] C. Svensson, et al., Coding of Experimental Conditions in Microfluidic Droplet Assays Using Colored Beads and Machine Learning Supported Image Analysis, Small (December) (2018) 1802384.
- [22] T. Wang, T.H. Kwok, C. Zhou, S. Vader, In-situ droplet inspection and closed-loop control system using machine learning for liquid metal jet printing, J. Manuf. Syst. 47 (April) (2018) 83–92.
- [23] W.T. Scott, Poisson Statistics in Distributions of Coalescing Droplets, J. Atmos. Sci. 24 (March (2)) (1967) 221–225.
- [24] M. Warshaw, Cloud Droplet Coalescence: Statistical Foundations and a One-Dimensional Sedimentation Model, J. Atmos. Sci. 24 (May (3)) (1967) 278–286.
- [25] J.W. Rose, Dropwise condensation theory, Int. J. Heat Mass Transf. 24 (2) (1981) 191–194.
- [26] H. Yang, Z. Zhang, J. Zhang, X.C. Zeng, Machine learning and artificial neural network prediction of interfacial thermal resistance between graphene and hexagonal boron nitride, Nanoscale 10 (40) (2018) 19092–19099.
- [27] F. Al-Obeidat, B. Spencer, O. Alfandi, Consistently accurate forecasts of temperature within buildings from sensor data using ridge and lasso regression, Futur. Gener.

- Comput. Syst. (2018).
- [28] C.S. Sanjaya, T.H. Wee, T. Tamilselvan, Regression analysis estimation of thermal conductivity using guarded-hot-plate apparatus, Appl. Therm. Eng. 31 (10) (2011) 1566–1575.
- [29] Y. Sun, L. Gu, C.F.J. Wu, G. Augenbroe, Exploring HVAC system sizing under uncertainty, Energy Build. 81 (2014) 243–252.
- [30] T. Zhan, L. Fang, Y. Xu, Prediction of thermal boundary resistance by the machine learning method, Sci. Rep. 7 (1) (2017) 1–2.
- [31] A.B. Gandhi, J.B. Joshi, V.K. Jayaraman, B.D. Kulkarni, Development of support vector regression (SVR)-based correlation for prediction of overall gas hold-up in bubble column reactors for various gas-liquid systems, Chem. Eng. Sci. 62 (24) (2007) 7078–7089.
- [32] M. Maalouf, D. Homouz, M. Abutayeh, Accurate prediction of preheat temperature in solar flash desalination systems using kernel ridge regression, J. Energy Eng. 142 (2) (2016) 1–7.
- [33] K.M. Tao, A closer look at the radial basis function (RBF) networks, 1993, 401–405.
- [34] C. Elbuken, T. Glawdel, D. Chan, C.L. Ren, Detection of microdroplet size and speed using capacitive sensors, Sensors Actuators A Phys. 171 (2) (2011) 55–62.
- [35] R. Dey, J. Gilbers, D. Baratian, H. Hoek, D. van den Ende, F. Mugele, Controlling shedding characteristics of condensate drops using electrowetting, Appl. Phys. Lett. 113 (2018).
- [36] I. Nayshevsky, Q. Xu, A.M. Lyons, Hydrophobic-Hydrophilic Surfaces Exhibiting Dropwise Condensation for Anti-Soiling Applications, IEEE J. Photovoltaics 9 (1) (2019) 302–307.